JOURNAL OF SPACECRAFT AND ROCKETS
Vol. 45, No. 5, September–October 2008

Experimental Study on Aerothermal Heating Caused by Jet-Hypersonic Crossflow Interaction

Ali Gülhan,* Gerrit Schütte,† and Bernhard Stahl*,‡
DLR, German Aerospace Research Center, 51147 Cologne, Germany

DOI: 10.2514/1.35899

The present paper reports on the results of an experimental study on aerothermodynamic effects associated with the injection of a lateral jet into a hypersonic crossflow around a generic missile model. This study intends to close the gap of missing reliable information on measured combined surface pressure and heat flux distribution on a missile configuration with a lateral jet. The model, consisting of a cone, cylindrical main body, and a flare, includes a single side jet hole. The model is made of a material with low thermal conductivity to visualize the surface temperature distribution, that is, heat fluxes. The surface temperature development on the model has been measured by infrared thermography. Using these data, the heat flux rate has been determined, taking into account temperature-dependent material characteristics, assuming a semi-infinite wall and the exchange of radiative cooling to the environment. Flow topology was analyzed using oil flow and schlieren images and wall pressure distribution measurements. The experimental data show that the jet pressure ratio has a significant effect on the side jet flow topology and its interaction with the crossflow. The influence of the angle of attack and the yaw angle on the pressure and heat flux distribution has also been measured clearly. Finally, the effect of various side jet gas media on the flow interaction has been demonstrated with tests using argon and helium as a jet gas complementary to air.

Nomenclature

a	=	thermal diffusivity, $m^2 \cdot s^{-1}$
a^*	=	speed of sound, $m \cdot s^{-1}$
C_p	=	pressure coefficient
c_p	=	specific heat capacity at constant pressure, $J \cdot g^{-1} \cdot K^{-1}$
D	=	diameter of the cylindrical part of model, mm
d_J	=	diameter of jet nozzle, mm
M_J	=	Mach number of the jet flow
M_∞	=	Mach number of the external flow
p	=	local pressure, bar
p_t	=	total pressure, bar
p_{0J}	=	pitot pressure at the jet exit, bar
p_∞	=	static pressure of the external flow, bar
q	=	dynamic pressure, bar
q_{conv}	=	convective flux
q_L	=	conductive heat flux
q_{rad}	=	radiative heat flux
Re	=	Reynolds number based on m^{-1}
St	=	Stanton number
T_J	=	static temperature of jet flow, K
T_t	=	total temperature of crossflow, K
T_∞	=	static temperature of the external flow, K
t	=	time, s
U_∞	=	velocity of external flow, $m \cdot s^{-1}$
x, y	=	Cartesian coordinates
z	=	thickness of polyether ether ketone material, mm
α	=	angle of incidence, respectively, heat-transmission coefficient
α_{therm}	=	coefficient of linear thermal expansion, K^{-1}
β	=	angle of yaw
ε	=	emission coefficient
κ	=	isentropic coefficient
λ	=	thermal conductivity, $W \cdot m^{-1} \cdot K^{-1}$
ρ	=	density, $kg \cdot m^{-3}$
σ_B	=	Stefan-Boltzmann constant, $J \cdot K^{-1}$
φ	=	circumferential angle

Subscripts

i	=	index (position)
J	=	jet
j	=	index (time)
ref	=	reference value
U	=	ambiance
W	=	wall
0	=	stagnation condition
∞	=	freestream

Received 28 November 2007; revision received 11 April 2008; accepted for publication 15 April 2008.

*Head of Department, Research Scientist, Wind Tunnel Department of the Institute of Aerodynamic and Flow Technology, Linder Höhe; ali.guelhan@dlr.de. AIAA Member.

†Research Scientist; currently Institute of Aircraft Propulsion Systems, University of Stuttgart; gerrit.schuette@ila.uni-stuttgart.de.

‡Research Scientist, Wind Tunnel Department of the Institute of Aerodynamic and Flow Technology, Linder Höhe; bernhard.stahl@dlr.de.

I. Introduction

THE missile systems of the future are being increasingly designed for enhanced maneuverability and higher agility. The associated demand for missile control can be addressed via side jet control solutions. The advantage of this method is that the exhaust jets can provide precise control forces with a very short response time. Compared to aerodynamic control surfaces, the advantages of side jet control are undisputed, particularly at low stagnation pressures in the launch phase and at high altitudes with low-pressure levels [1,2]. In its passive state, side jet control produces no additional drag because no components intrude into the flow stream. On the other hand, control systems with ailerons and rudders work more efficiently at high velocities and high densities.

The prediction of jet–crossflow interaction with the missile's fuselage flow boundary layer is limited in practical applications. A review of investigations into side jet interaction with a supersonic crossflow is given in Champigny and Lacau [3]. The flow topology is represented in the schematic of Fig. 1. The interaction area is characterized essentially by a separation region upstream of the jet, a three-dimensional bow shock generated immediately in front of the side jet, and counterrotating vortex pairs forming in the wake.

The jet plume itself is enclosed by a barrel shock and the Mach disc. Its inclination depends on the freestream velocity, penetration

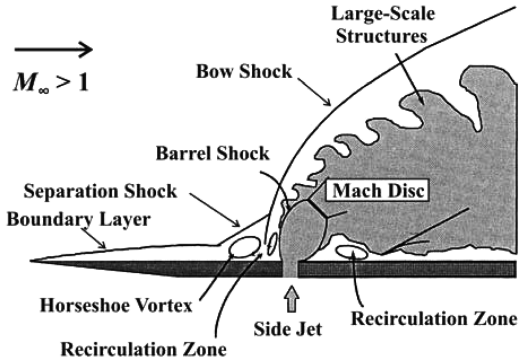

a)

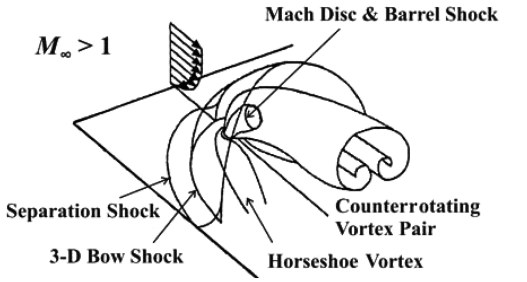

b)

Fig. 1 Schematic of transverse injection into a supersonic flowfield: a) side view at jet centerline axis and b) 3-D perspective (Ben-Yakar et al. [23]).

depth in relation to the jet pressure ratio, and flight altitude. With increasing altitude, and hence lower pressure densities, the side jet erects itself increasingly into the freestream [4]. The counterrotating vortices are generated downstream of the barrel shock. By visualizing the flow in the wake of a side jet, Fric and Roshko [5] have demonstrated the development of counterrotating vortex pairs. Steven et al. [6] have used particle image velocimetry to measure the mean vector fields in the far field of the interaction area and varied the jet-to-freestream dynamic pressure ratio and crossflow Mach number. The presence of the decaying jet and the induced counterrotating vortex pair were evident from measurements of streamwise and vertical components of mean velocity. Gruber et al. [7,8] have proven that the vortex size depends to a very great extent both on the jet gas (in this case, helium and air) and on the nozzle shape (round or elliptical). The separation of the boundary layer in front of the jet is due to the pressure rise and induces a horseshoe vortex that wraps itself around the side jet. This is the area of induced high pressure. Further vortices may form in the separation region; their number depends primary on the jet pressure ratio and angle of attack. According to the two-dimensional numerical simulation of Qin and Redlich [9], four vortices occur in the separation region in front of the jet at the pressure ratio $p_{0J}/p_\infty = 342$ and $M_\infty = 6.69$. In the recirculation zone, downstream of the jet, there exists a pronounced area of low pressure, which may compensate for the induced effect of the high-pressure area upstream and to the side of the jet. If high pressure predominates integrally in the jet's interaction area, one can speak of a thrust amplification effect and of a force amplification factor $K_F > 1$ [10–12]. Experimental and numerical investigations of the interaction between a lateral jet with a supersonic crossflow are given in Gnemmi and Schäfer [13] and Gnemmi et al. [14]. Surface pressure measurements are used to validate the computations for different jet pressure ratios. The close match has permitted the calculation of force and moment amplification factors. Using pressure-sensitive paint measurements, Gruber and Goss [15] have detected the pressure field in the region of jet–crossflow interaction and have used profiles of the pressure distributions to show the extent of the low-pressure areas for different jet pressure ratios of round and elliptical nozzles.

Although several numerical and experimental studies are available on the flow topology and pressure distribution of the side jet–crossflow interaction, there is a lack of reliable information with respect to the aerothermal heating caused by the side jet—hypersonic-crossflow interaction. Such studies require well-calibrated experimental tools, such as a reliable software to deduce heat flux rate from measured surface temperature distribution and a hypersonic wind tunnel with well-characterized flowfield. At the DLR wind-tunnel department, a technique for the heat flux determination from measured surface temperature distribution with an infrared (IR) camera using an in-house data reduction code have been established and is in use for several similar applications [16,17]. Because of its broad operation range at total temperatures up to 1100 K and test duration of 30 s, the DLR Hypersonic Wind Tunnel (H2K) offers good opportunities to perform aerothermal studies. Based on these boundary conditions, this study has been performed with a focus on the aerothermal heating caused by the jet–crossflow interaction. In addition to the surface temperature and surface pressure measurements, schlieren and oil flow techniques are used to visualize the flow topology.

II. Experimental Tools and Test Parameters

The experiments were carried out at the DLR Hypersonic Wind Tunnel and Trisonic Wind Tunnel (TMK) facilities in Cologne. The H2K, shown in Fig. 2, is an intermittent blowdown tunnel for hypersonic flows. It uses contoured, axially symmetrical, and replaceable nozzles. For aerodynamic testing, nozzles for Mach numbers of 4.8, 5.3, 6.0, 7.0, 8.7, and 11.2 are available. The diameter of the nozzles is 0.6 m (0.36 m at $M_\infty = 4.8$). To achieve the pressure ratio required to build up a jet flow for approximately 30 s, the pressure in the test chamber is reduced by means of a vacuum sphere. Because of the intense expansion of the air in the nozzle, its static temperature decreases significantly. To prevent condensation of air particles, and for tests at high temperatures, the air is preheated. Eight electric heaters with a maximum electrical power of 5 MW heat the air up to 1100 K. The maximum total pressure is 55 bar.

The TMK is a blowdown wind tunnel and has a cross-sectional area of 0.6×0.6 m. It is equipped with a flexible nozzle. The standard Mach number range is $1.25 < M_\infty < 4.5$. Mach numbers up to 5.7 can be reached by means of a storage heater and an ejector. For Mach numbers of $0.5 < M_\infty < 1.2$, a transonic test section with perforated walls is available. The wind tunnel is operated at a static pressure $p_\infty \approx 1$ bar for $M_\infty < 1.2$ and at a dynamic pressure of $q_\infty \approx 1$ bar for $M_\infty > 1.2$. The maximum running time, depending on Mach and Reynolds numbers, is up to 60 s. The TMK and its capabilities are described in more detail in [18].

The measurements were carried out with different jet gases in an air crossflow under the test conditions given in Table 1.

A. Generic Missile Model

For the investigations in the side jet interaction area, a generic wind-tunnel model was employed which comprises the classical missile components of the cone, cylindrical fuselage, and flare (Fig. 3).

The outer diameter of the cylindrical fuselage component is $D = 40$ mm and its length is 3.2 diameters. The model cone has a length of 2.8 diameters, whereas that of the flare is 3 diameters. The cylindrical jet nozzle is positioned at $\varphi = 180$ deg and 4.3 diameters downstream of the cone tip. For air as jet gas, at the exit of the nozzle, the Mach number is $M_J = 1$ and the temperature is $T_J = 244$ K. To

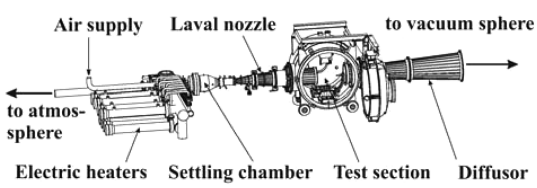

Fig. 2 Hypersonic wind tunnel (H2K).

Table 1 Test parameters

M_∞	T_t, K	p_∞, bar	p_t, bar	Jet gas	p_{0J}/p_∞	α, deg	β, deg	Re
				H2K				
5.3	$352 \le T_t \le 415$	0.0107	8.0	Air	$50 \le p_{0J}/p_\infty \le 300$	−10, 0, 10	5, 10	$12 \le Re \cdot 10^{-6} \le 15$
5.3	415	0.0107	8.0	Helium	100, 300	0 deg	0 deg	12
5.3	415	0.0107	8.0	Argon	100, 300	0 deg	0 deg	12
				TMK				
5.3	295	0.0153	8.0	Air	100, 300	0 deg	0 deg	19

measure the pressure distribution on the model surface, the model has 11 static pressure taps with a diameter of 0.5 mm ($\varphi = 180$ deg).

Because the focus of this research is on determining and interpreting the heat transmission on the surface of the model, the material of the model must meet specific requirements. Thus, for a convective heat flux determination, the unsteady-state heat conduction equation is considered to be one-dimensional, that is, the aspect of cross-heat conduction is neglected. A material which fulfils this requirement is polyether ether ketone (PEEK), given its low thermal conductivity. PEEK is a linear aromatic polymer of high mechanical resistance. Apart from its ability to withstand chemical attack and hydrolysis, it qualifies for use in aerothermodynamic research particularly due to its thermal properties at high temperatures. Key characteristics to be emphasized in this context are its relatively high melting temperature of 616 K, its maximum continuous temperature of 533 K, its low thermal conductivity of $\lambda = 0.258\ \mathrm{W \cdot m^{-1} \cdot K^{-1}}$, and thermal diffusivity $a = 19.23 \times 10^{-8}\ \mathrm{m^2 \cdot s^{-1}}$ at 293 K.

Another boundary condition to be ensured is the assumed semi-infinite wall thickness of the model. In other words, the wall thickness must be chosen such that the heat flux applied to the model surface will not be noticeable on the underside during the time of the test. Using the equation for the dimensionless temperature field

$$\frac{T(x,t) - T_w}{T_U - T_w} = 1 - \frac{2}{\sqrt{\pi}} \int_{\xi=0}^{\xi=\eta} e^{-\xi^2}\, \mathrm{d}\xi \tag{1}$$

and applying the Gaussian error function, the wall thickness condition can be determined as

$$z(t) = 4 \cdot \sqrt{a(T_w) \cdot t} \tag{2}$$

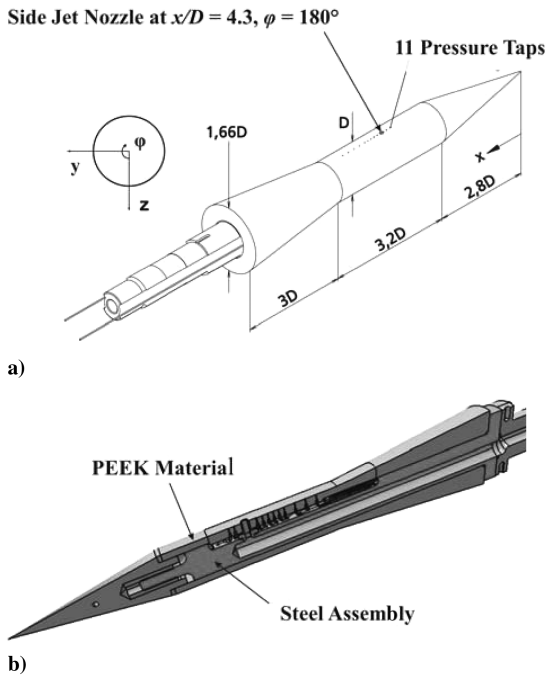

Fig. 3 Wind-tunnel model with side jet nozzle and static pressure taps: a) dimensions of the model and b) cross-sectional view of the model.

At a maximum test duration of 20 s and the maximum continuous temperature of 533 K, the maximum penetration depth amounts to $z = 6$ mm. The wall thickness of the PEEK material in the side jet interaction area was selected to be >6.3 mm. To make the model resistant against dynamic pressure, inherent pressures, and thrust, it was internally reinforced with a steel (42CrMo4) skeleton structure (see cross-sectional view in Fig. 3).

B. Pressure Measurements

Wall pressure measurements were carried out on the PEEK model in the H2K and, additionally, on a steel model of the same geometry that was used in the TMK. The steel model is equipped with 148 static pressure taps, each measuring 0.5 mm in diameter. The taps are positioned in four longitudinal sections at the circumferential angles $\varphi = 180, 150, 120$, and 90 deg. A detailed description of the model is given in [19].

The wall pressures measured on the PEEK model served to validate the pressures recorded on the steel model. Although the surface temperatures of the models differ as a result of dissimilar heat-transmission conditions, and their Reynolds numbers do not match exactly, the wall pressure readings showed a high degree of coincidence (see Table 2). The pressure taps were connected to pressure scanners [Pressure Systems, Inc. (PSI) system 8400]. The static accuracy of the PSI modules is ±0.1% of the full-scale deflection. Measurement errors due to Mach number deviations and changes in the freestream angle are generally greater. In the TMK, local pressure deviations as a consequence of ΔM_∞ of $\Delta C_p = \pm 0.004$ and due to $\Delta\alpha$ deviations of $\Delta C_p = \pm 0.003$ may occur.

C. Schlieren Optic and Oil Film Technique

For the flow visualization in H2K, a coincidence schlieren system was used. The schlieren images were focused directly into a camera.

To visualize the interaction of the side jets with the freestream on the model surface by means of wall streamlines, oil flow pictures were taken. To this end, an adhesive film was placed on the model to protect the pressure taps, and a mixture of oil, petroleum, and fluorescent pigments was applied to this film.

D. Infrared Thermography

The signal detected by a thermocamera depends mainly on the temperature T of the thermographed body and its emission coefficient. The ThermaCAM 300 camera system employed for our purposes uses a quantum-well-infrared-photon (QWIP) detector with 320 × 240 pixels and 60 Hz, operating in the long-wave infrared range (8–9 μm) at temperatures between −20 and 2000°C. The camera has different calibrated measurement ranges. During this test campaign, the measurement range of 10–150°C was used. The variance of the emission coefficient is negligible in this temperature range. The emission coefficient of the PEEK model was $\varepsilon = 0.95$.

Table 2 Parameters of pressure measurements in the H2K and TMK

M_∞	Re	T_t, K	p_t, bar	q, bar
		H2K		
5.3	15×10^6	352	8.0	0.21
		TMK		
5.3	19×10^6	295	8.0	0.21

An estimate of the measurement error caused by the angle of the camera's optical axis to a reference line vertical to the model yields a minor deviation of 1% at angles of observation below 50 deg. At larger angles, appreciable distortions are observed. The evaluation of the IR measurements was therefore restricted to angles up to ±45 deg. This corresponds to circumferential angles of $135 < \varphi < 225$ deg on the model.

III. Heat Flux and Stanton Number

For the determination of the convective heat flux, the heat flux balance on the model surface is considered locally in one dimension. Given the low heat conductivity of the PEEK material, heat conduction is negligible. At any point of the model surface, the heat flux is

$$\dot{q}_L = \dot{q}_{\text{conv}} - \dot{q}_{\text{rad}} \tag{3}$$

where q_L denotes heat conduction within the material, q_{conv} stands for the convective heat flux, and q_{rad} is the radiative cooling. The heat flux radiated into the test section, that is,

$$\dot{q}_{\text{rad}} = \varepsilon \cdot \sigma_B \cdot (T_W^4 - T_U^4) \tag{4}$$

shows a high dependency on the wall temperature and ambient temperature.

Because the material behavior in terms of heat capacity and thermal conductivity varies with local temperature, the unsteady-state heat conduction equation becomes

$$\rho \cdot c_p \cdot \frac{\partial T}{\partial t} = \frac{\partial \lambda}{\partial z} \cdot \frac{\partial T}{\partial z} + \lambda \frac{\partial^2 T}{\partial z^2} \tag{5}$$

This differential temperature expression is a function not merely of place and time, but also of the density ρ, the thermal conductivity λ, and the specific heat capacity c_p. In the interests of reliable results, an accurate knowledge of material characteristics and their behavior under temperature variation is therefore essential. The temperature dependency of the individual parameters, related to the reference values at $T_{\text{ref}} = 293$ K, $c_{p,\text{ref}} = 1.039\ \text{J} \cdot \text{g}^{-1} \cdot \text{K}^{-1}$, $\lambda_{\text{ref}} = 0.258\ \text{W} \cdot \text{m}^{-1} \cdot \text{K}^{-1}$, and $a_{\text{ref}} = 19.23 \times 10^{-8}\ \text{m}^2 \cdot \text{s}^{-1}$, is plotted in Fig. 4 up to a maximum continuous temperature of 533 K. The characteristics of the PEEK material were determined at the DLR Institute of Materials Research, Cologne.

In particular, the PEEK coefficients $c_p/c_{p,\text{ref}}$ and a/a_{ref} show a significant dependence on temperature. The coefficients were approximated polynomial and considered during calculation of the Stanton number. To determine the values of λ and a, three tests were conducted in each case at similar temperatures. The density ρ is deemed to be linear over the temperature range examined and is described by

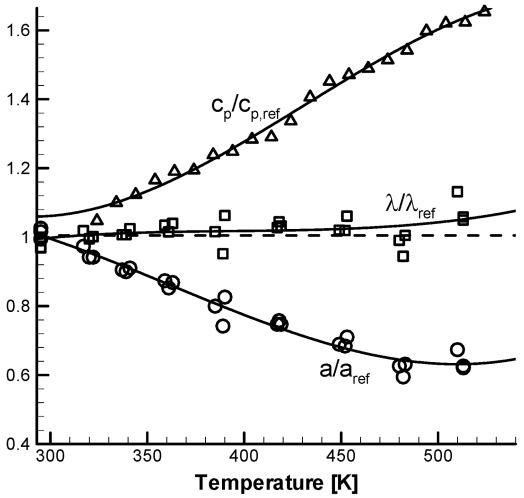

Fig. 4 Relative temperature dependency of material properties.

$$\rho = \rho_{\text{ref}} + \alpha_{\text{therm}} \cdot T \tag{6}$$

The coefficient of linear thermal expansion is $\alpha_{\text{therm}} = 1.2 \times 10^{-5}\ \text{K}^{-1}$, and the reference density is $\rho_{\text{ref}} = 1.29\ \text{kg} \cdot \text{m}^{-3}$.

For an explicit solution of the one-dimensional heat conduction equation, the material properties are approximated by polynomials. A homogeneous temperature distribution within the model and a semi-infinite wall are assumed as boundary conditions. Taking into account heat loss by radiation, the convective heat flux on the surface of the model can be written as

$$\dot{q}_{\text{conv}} = -\lambda \cdot \left.\frac{\text{d}T}{\text{d}z}\right|_{z=0} + \varepsilon \cdot \sigma_B \cdot (T_W^4 - T_U^4) \tag{7}$$

The resulting Stanton number characterizing the convective heat transmission has been related to flow conditions by

$$St = \frac{\dot{q}_{\text{conv}}}{\rho_\infty \cdot U_\infty \cdot c_{p,\text{air}} \cdot (T_t - T_{i-0,j})} \tag{8}$$

in the present research, as proposed by Abgrall et al. in [20]. $T_{i=0,j}$ is determined by the infrared measurements.

For the convective heat flux calculation, the uncertainty of the measured absolute temperature value is noncritical, whereas the temperature gradient over time is the most important parameter. A sensitivity analysis has been performed for the Stanton number accuracy using PEEK material data and wind-tunnel conditions. With consideration of the error range of each parameter of the Stanton number $St = f\ (M_\infty,\ p_t,\ T_t,\ T_{i=0,j},\ q_{\text{conv}})$, the 2^5 combinations have been calculated. The result shows that, for the worst case, that is, maximum error in all parameters, the overall accuracy of the Stanton number is ±15%. The error of the convective heat flux is a maximum of ±5% based on the uncertainties in the PEEK material properties.

IV. Experimental Results

The expansion of a side jet injected into a hypersonic crossflow generates an exceptionally complex flowfield. Both the pressure and heat flux distributions are strongly influenced by the side jet. The pressure distribution defines the efficiency of the side jet and it also helps, together with the heat flux distribution, to evaluate the thermal fluid structure interaction and structural performance of the vehicle. In the presented aerothermodynamic study, the convective heat flux to the surface of the model is determined and expressed in terms of Stanton number distributions. The upper part of Fig. 5 shows the distribution of Stanton numbers and wall pressures at circumferential

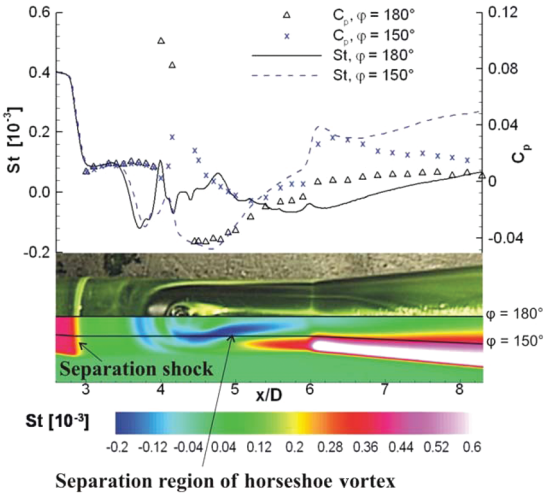

Fig. 5 Stanton number, oil film picture, and Stanton number distribution, measured at $M_\infty = 5.3$, $Re = 15 \times 10^6\ \text{m}^{-1}$, $p_{0J}/p_\infty = 300$, $\alpha = 0$ deg, $T_t = 352$ K, wall pressure measured at $Re = 19 \times 10^6\ \text{m}^{-1}$, $p_{0J}/p_\infty = 300$, $T_t = 295$ K.

angles $\varphi = 180$ and 150 deg in each case. The lower part of this illustration gives the associated oil film image (from the top half of the model) and the projected Stanton number distribution. The wall pressure distributions reveal an overpressure in the separation region in front of the air jet, which rises to a substantial peak at the bow shock site. Near the recirculation of the wake, we can identify a low pressure which converges toward zero by the time it reaches the cylinder-to-flare transition area. On the flare itself, an overpressure prevails. As is evident from the oil film image and the Stanton number distribution, the separation shock forms at the cone shoulder. Downstream, the Stanton numbers drop sharply to a plateau, followed by another drop caused by the separated horseshoe vortex. Upon reattachment of the vortex, the Stanton number ($\varphi = 180$ deg) shows a pronounced peak. Downstream of the injection site, the Stanton numbers rise again, reflecting the fact that the temperature of the jet exceeds that of the freestream. At both circumferential angles, the Stanton numbers are similar up to the formation of the horseshoe vortex. In the area adjacent to the jet, on the other hand, the Stanton numbers exhibit major differences in the circumferential direction. At $\varphi = 150$ deg, in the region of the horseshoe vortex wrapped around the jet, the heat transfer is less intense, with Stanton numbers reaching a pronounced minimum from there. Further downstream, outside the area affected by the horseshoe vortex, the Stanton numbers rise markedly due to the impact, or deflection, of the freestream in the peripheral area of the flare.

Figure 6 shows the associated schlieren scan in lieu of the oil film image alongside the Stanton number diagram. It is evident from the schlieren image that the separation area in front of the jet extends all the way to the cone shoulder. Also apparent are the shocks shown schematically in Fig. 1.

A. Effect of Jet Pressure Ratio

The jet pressure ratio of the air side jet was varied in a $50 \leq p_{0J}/p_\infty \leq 300$ range. As the pressure ratio increases, the separated overpressure region in front of the jet moves steadily upstream while the lower pressure region in the wake extends over a larger area [19]. In the control of missiles via side jets, the transverse thrust system becomes more effective with increasing jet pressure ratio. This effect is attributable to the thrust-amplifying overpressure in front of the jet, whereas the lower pressure counteracting the thrust contributes less to the overall pressure level in the interaction area. Figure 7 gives the Stanton number profile, the oil film image, and the Stanton number distribution recorded at a lower jet pressure ratio $p_{0J}/p_\infty = 100$. A comparison with Fig. 5 reveals a smaller separation area, marked by the wide yellow line in the oil film picture. Accordingly, the maxima of the Stanton number profile are oriented more closely around the

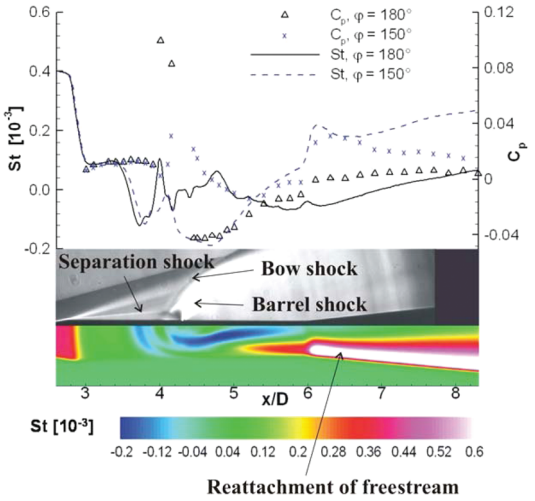

Fig. 6 Stanton number, schlieren image, and Stanton number distribution, measured at $M_\infty = 5.3$, $Re = 15 \times 10^6$ m^{-1}, $p_{0J}/p_\infty = 300$, $\alpha = 0$ deg, $T_t = 352$ K, wall pressure measured at $Re = 19 \times 10^6$ m^{-1}, $p_{0J}/p_\infty = 300$, $T_t = 295$ K.

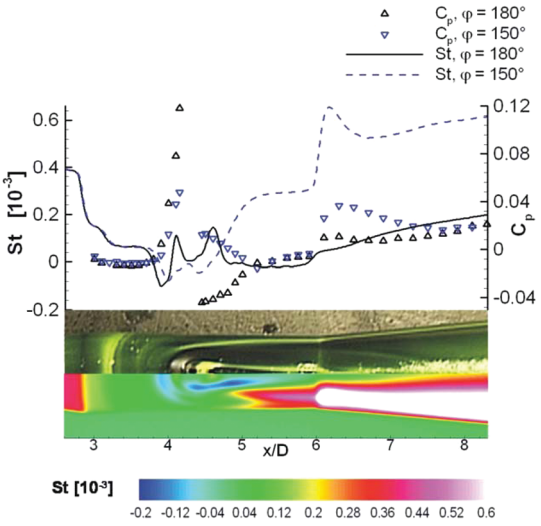

Fig. 7 Stanton number, oil film picture, and Stanton number distribution, measured at $M_\infty = 5.3$, $Re = 15 \times 10^6$ m^{-1}, $p_{0J}/p_\infty = 100$, $\alpha = 0$ deg, $T_t = 352$ K, wall pressure measured at $Re = 19 \times 10^6$ m^{-1}, $p_{0J}/p_\infty = 100$, $T_t = 295$ K.

jet. At $\varphi = 150$ deg, a substantial increase in Stanton numbers commences as early as at the jet exit site. The numbers then rise sharply at the cylinder-to-flare transition point.

From the schlieren images juxtaposed in Fig. 8, it can be seen that, as the jet pressure ratio increases, the separated area in front of the jet moves upstream, the bow shock shows a steeper rise, the air jet penetrates more deeply into the freestream, and the barrel shock increases greatly in magnitude. The position of the separated area in front of the jet is clearly indicated in the Stanton number distributions in Fig. 9 by the color transition from green to turquoise. Moreover, apart from the schlieren image pattern, the extension of the interaction area in the circumferential direction becomes evident. The horseshoe vortex enclosing the air jet shows a constriction on the downstream side caused by the lower pressure in the recirculation area. At low jet pressure ratios, the high-turbulence wake portion is limited to a fairly narrow region. In the flare edge areas, on the other

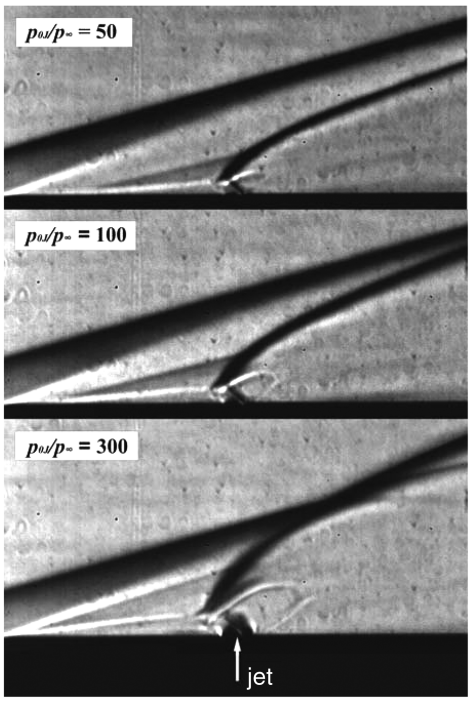

Fig. 8 Schlieren images at different jet pressure ratios, measured at $M_\infty = 5.3$, $Re = 15 \times 10^6$ m^{-1}, $\alpha = 0$ deg, $T_t = 352$ K.

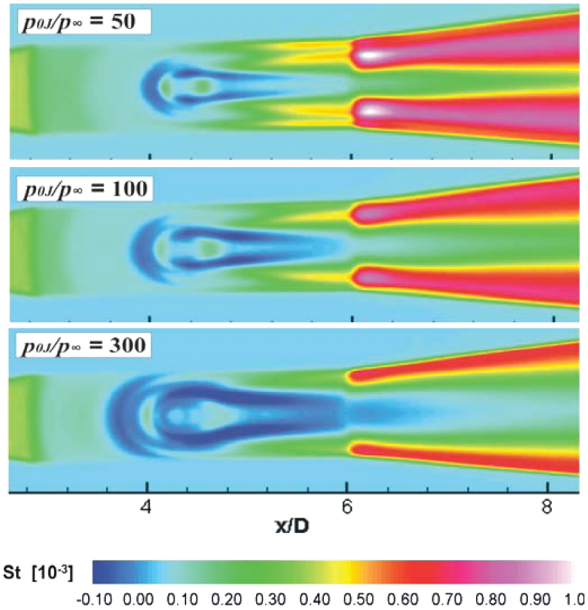

Fig. 9 Stanton number distribution at different jet pressure ratios, measured at $M_\infty = 5.3$, $Re = 15 \times 10^6$ m^{-1}, $\alpha = 0$ deg, $T_t = 352$ K.

hand, an intense heat transfer can be observed due to the freestream. With increasing jet pressure ratio, the heat flux in front and in the wake of the side jet extends over a larger interaction surface.

The Stanton numbers compared in Fig. 10 show a similar pattern in front of the air jet, with a shift toward the upstream side as the jet pressure ratio increases. Starting from the cylinder-to-flare transition, the Stanton numbers rise substantially, particularly at low jet pressure ratios, as the heat flux induced by the free flow becomes a stronger influence here.

B. Effect of Angle of Attack and Angle of Yaw

Figure 11 shows the schlieren images recorded at angles of attack $\alpha = 0$, -10, and 10 deg. At $\alpha = 0$ deg, the separation shock is generated at the cone shoulder, whereas with windward injection ($\alpha = -10$ deg), the separation area is limited to a very small region of high wall pressure in front of the air jet [19]. In a leeward injection ($\alpha = 10$ deg) configuration, the separation shock sets in just behind the cone shoulder.

Figure 12 gives the Stanton number profiles recorded for $\alpha = -10$ deg, the oil film image, and the Stanton number distribution. In the area before the air jet, the separation shock is generated at $x/D = 3.6$, whereas in the $\alpha = 0$ deg setup it already occurred on the cone shoulder at $x/D = 2.8$. The Stanton number profiles tend to show a pattern similar to the tests with zero attack angle ($\alpha = 0$ deg, see Fig. 5), but on a substantially higher level. In

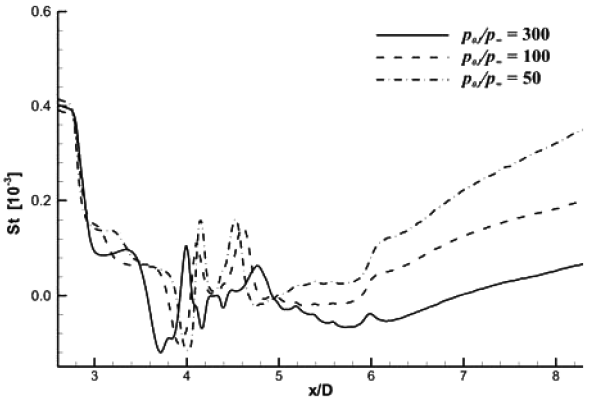

Fig. 10 Stanton number at different jet pressure ratios, measured at $M_\infty = 5.3$, $Re = 15 \times 10^6$ m^{-1}, $\alpha = 0$ deg, $\varphi = 180$ deg, $T_t = 352$ K.

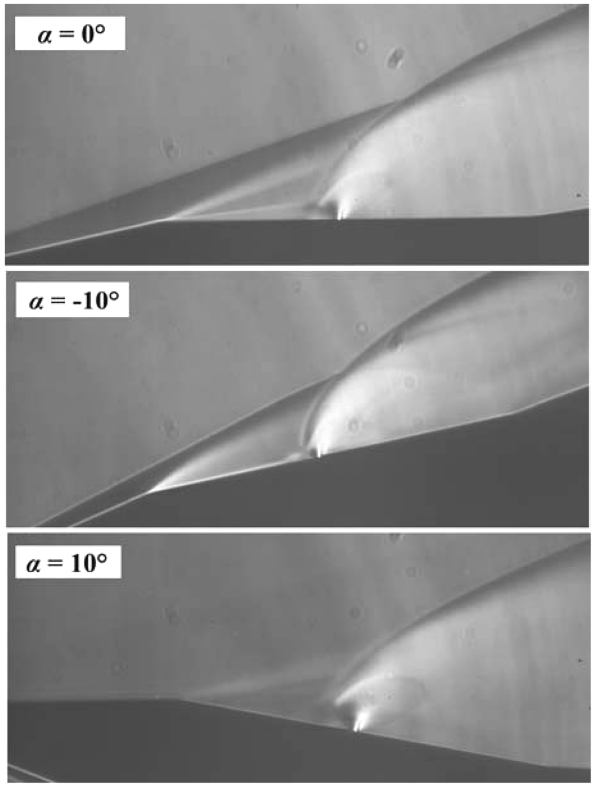

Fig. 11 Schlieren images at different angles of attack, measured at $M_\infty = 5.3$, $Re = 12 \times 10^6$ m^{-1}, $p_{0J}/p_\infty = 300$, $T_t = 415$ K.

the horseshoe vortex area, the Stanton number peak exceeds its counterpart in the $\alpha = 0$ deg configuration by a factor of 5. The oil film image shows the horseshoe vortex separation line marked by the yellow line which wraps around the fuselage in an outward direction.

Figure 13 illustrates the corresponding flow parameters determined for $\alpha = 10$ deg. As is evident from the oil film image and from the distribution of Stanton numbers, the separation area before the air jet has its maximum extension upstream at $\varphi \approx 120$ deg, whereas, in the jet axis at $\varphi = 180$ deg, this site is located somewhat further downstream [21]. Because of the positive angle of attack, the area under the separation shock is greater, with the volume of the horseshoe vortex increasing accordingly.

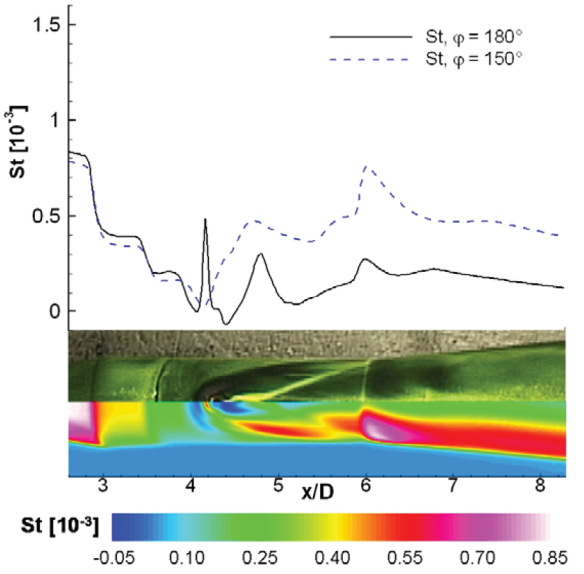

Fig. 12 Stanton number, oil film picture, and Stanton number distribution, measured at $M_\infty = 5.3$, $Re = 12 \times 10^6$ m^{-1}, $p_{0J}/p_\infty = 300$, $\alpha = -10$ deg, $T_t = 415$ K.

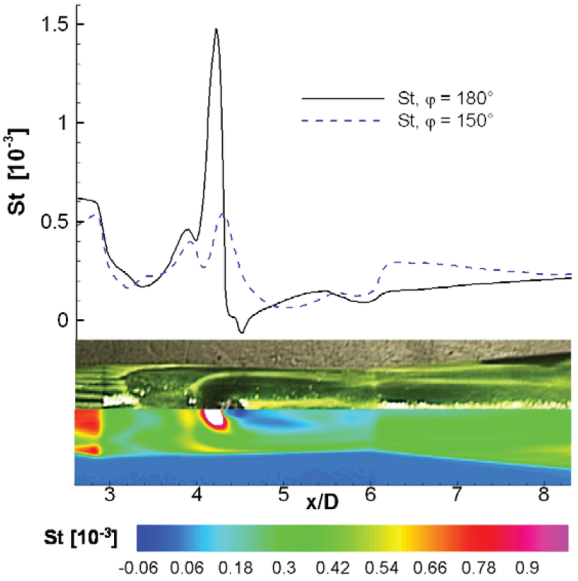

Fig. 13 Stanton number, oil film picture, and Stanton number distribution, measured at $M_\infty = 5.3, Re = 12 \times 10^6$ m^{-1}, $p_{0J}/p_\infty = 300$, $\alpha = 10$ deg, $T_t = 415$ K.

Substantial heat transfer takes place in this region, exceeding the maximum determined with $\alpha = 0$ deg by a factor of 15 (see Fig. 5). On the flare, no rise in heat flux is evident as a result of the leeward freestream.

Figure 14 gives the Stanton number profiles determined at various angles of attack. Significant differences in heat transfer can be identified, especially in the horseshoe vortex area. In the $\alpha = 10$ deg configuration, the spatial extension of the horseshoe vortex is indicated by the substantial heat transfer taking place in front of the jet. Viewed against the other configurations, the input of heat is intensified here as a result of the extensive horseshoe vortex. Behind the jet, on the other hand, the Stanton numbers are affected much less by the angle of attack.

Figure 15 illustrates the effect of the angle of yaw on the Stanton numbers and their distribution. The Stanton number distribution reflects the asymmetrical heat flux resulting from the oblique oncoming flow. Even at the cone shoulder, the separation shock is not generated symmetrically. With $\varphi = 150$ deg, the Stanton number profile reaches its peak at the tip of the model, that is, outside the interaction area of the air side jet. The position of the separation shock likewise varies greatly in the circumferential direction, as

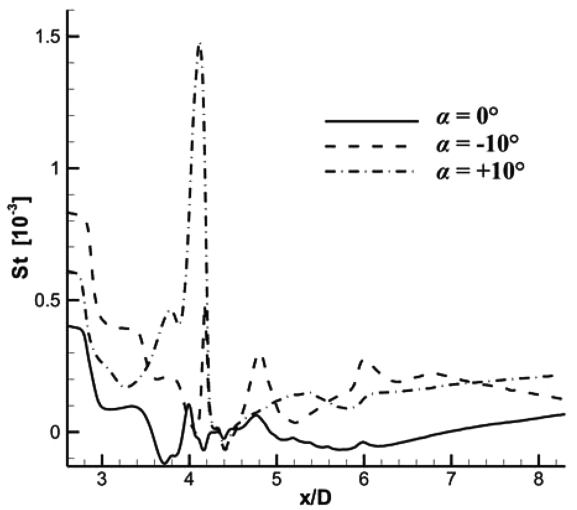

Fig. 14 Stanton number at different angles of attack, measured at $M_\infty = 5.3$, $Re = 12 \times 10^6$ m^{-1}, $p_{0J}/p_\infty = 300$, $\varphi = 180$ deg, $T_t = 415$ K.

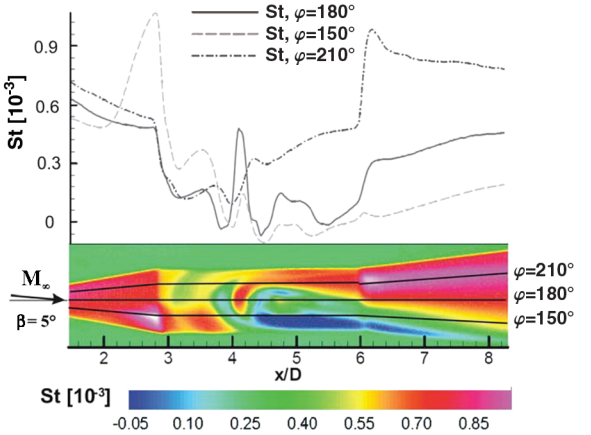

Fig. 15 Effect of angle of yaw on Stanton number and Stanton number distribution, measured at $M_\infty = 5.3$, $\varphi = 180$ deg, $p_{0J}/p_\infty = 300$, $\alpha = 0$ deg, $\beta = 5$ deg, $T_t = 415$ K.

indicated by the yellow line. Overall, the heat flux is more intense on the windward (at $\varphi = 210$ deg) when compared with the separated leeward side (at $\varphi = 150$ deg). At a still greater angle of yaw ($\beta = 10$ deg), the previously described effects are more pronounced, as can be seen in Fig. 16.

C. Effect of Helium, Argon, and Air Side Jet

A key difference in the material properties of the jet gases examined lies in their density, which is 10 times higher for argon than in the case of helium. As a result, major dissimilarities in both the mass flow and volumetric flow rates of the jet are encountered at a constant jet pressure ratio p_{0J}/p_∞. The material properties of the gas media are summarized in Table 3. It is evident from these figures that the jet mass flow is greatest with argon, whereas the volumetric flow rate and hence the velocity of the jet are many times higher with helium than with argon or air. The schlieren images in Fig. 17 attest to the widely varying barrel shock magnitudes at the same jet pressure ratio. The helium barrel shock is barely visible due to its low density.

Figure 18 gives the oil film images and Stanton number distributions recorded with a helium, argon, and air jet. Because of the great dissimilarities in volumetric flow rate and jet expansion behaviors, the Stanton number distributions reflect considerable differences in heat transfer to the model surface in the interaction region. Accelerating the gas flow in the nozzle reduces the temperature of the exiting jet, with internal energy being converted into kinetic energy. This static temperature drop is more pronounced

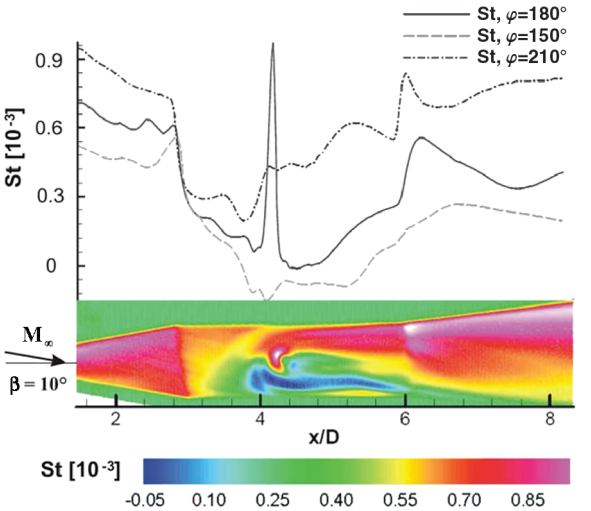

Fig. 16 Effect of angle of yaw on Stanton number and Stanton number distribution, measured at $M_\infty = 5.3, Re = 12 \times 10^6$ m^{-1}, $p_{0J}/p_\infty = 300$, $\alpha = 0$ deg, $\beta = 10$ deg, $T_t = 415$ K.

Table 3 Properties of the jet gases

		Helium	Argon	Air
c_p	$J \cdot kg^{-1} \cdot K^{-1}$	5230	523	1005
c_V	$J \cdot kg^{-1} \cdot K^{-1}$	3209	317	717
$C_{M,p}$	$J \cdot mol^{-1}K^{-1}$	20.79	20.79	29.1
κ	——	1.63	1.648	1.402
R	$J \cdot kg^{-1} \cdot K^{-1}$	2077	208.1	287.1
ρ	$kg \cdot m^{-3}$	0.1785	1.784	1.275
$\dot{m}$	$kg \cdot s^{-1}$	0.0371	0.118	0.0954
$\dot{V}$	$m^3 \cdot s^{-1}$	0.208	0.066	0.0748
U_{Jet}	$m \cdot s^{-1}$	914.8	291.0	310.5
$a^*/\sqrt{T_J}$	$m \cdot s^{-1} \cdot (K^{-1})^{1/2}$	58.2	18.5	20.0

in the case of the helium jet, given its high velocity, than it is with argon or air. As a result, heat transfer is very low both in the area around the helium jet itself and further downstream up to the end of the flare. Exiting at $M_J = 1$, the helium jet has a very high sound velocity (refer to Table 3) or outlet velocity, respectively, which, at $U_{J,\text{He}} = 901\ m \cdot s^{-1}$, exceeds the freestream velocity $U_\infty = 841\ m \cdot s^{-1}$. The separation lines are documented in the oil film images. The separation shock occurs at $x/D \approx 3.20$ in the case of the argon jet, at $x/D \approx 3.03$ in the case of the air jet, and at $x/D \approx 2.98$ in the case of the helium jet.

Figure 19 shows the Stanton number profiles for different gas jets. With helium, the heat flux in the horseshoe vortex and jet wake areas is much lower than with the other jets. This result confirms the findings of Esch [22], who investigated the jet interference effect on wall pressures at $M_\infty = 2.8$ through extensive measurements with argon, helium, hydrogen, and ethane side jets on a geometrically identical model.

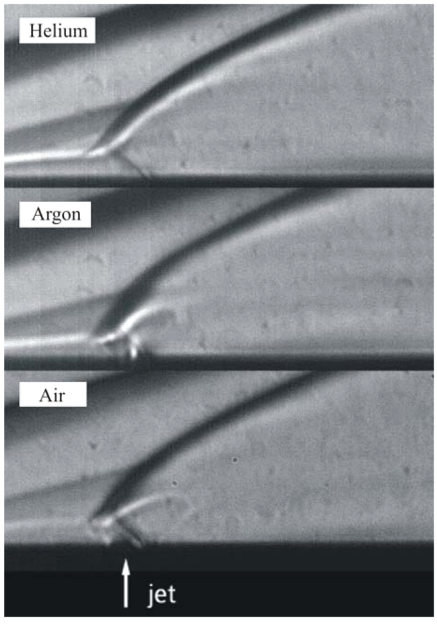

Fig. 17 Schlieren images, measured at different gas jets, $M_\infty = 5.3$, $Re = 12 \times 10^6\ m^{-1}$, $\alpha = 0$ deg, $p_{0J}/p_\infty = 100$, $T_t = 415$ K.

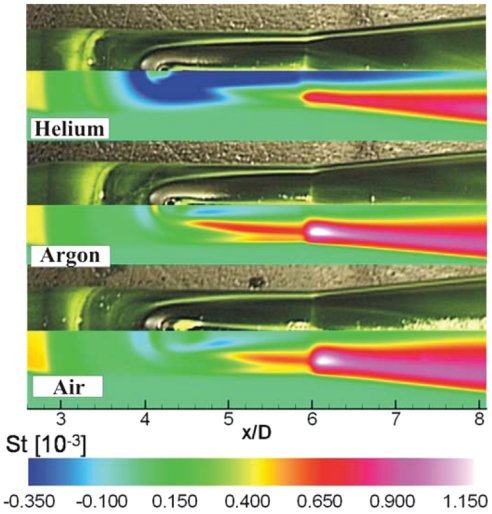

Fig. 18 Oil film pictures and Stanton number distributions, measured at different gas jets, $M_\infty = 5.3$°C, $Re = 12 \times 10^6\ m^{-1}$, $\alpha = 0$ deg, $p_{0J}/p_\infty = 100$, $T_t = 415$ K.

V. Conclusions

The aerothermodynamic effects associated with the injection of a side jet into a hypersonic crossflow were examined on a generic high-speed missile model. The convective heat flux from the flow stream to the model was determined from measured surface temperature development by solving a one-dimensional heat conduction equation, taking into account temperature-dependent material properties and the radiative cooling of the surface. Profiles of Stanton numbers in the stream axis and Stanton number distributions in the side jet interaction area are given. To permit a correlation of the aerothermodynamic effects, which are the focus of this investigation, with the aerodynamics of the complex flowfield, the flow topology was analyzed with the aid of wall pressure measurements, schlieren images, and oil film images. The jet pressure ratio, as well as the angle of attack and the model's angle of yaw, were varied. To study the interaction of various jet gases with the freestream in the interaction area, helium, argon, and air were used as jet gases.

1) Effect of jet pressure ratio: As the jet pressure ratio increases in a $50 \le p_{0J}/p_\infty \le 300$ range, the separated flow areas in front and in the wake of the side jet become larger. The Stanton number profiles indicate a dominant heat flux upon reattachment of the horseshoe vortex and in the recirculation zone in the wake of the jet. The maximum amplitudes of the Stanton number peaks were determined at $p_{0J}/p_\infty = 50$ because the jet's penetration depth into the freestream is small at this ratio. From the cylinder-to-flare transition area, the heat transfer increases substantially because, here, the heat flux is determined largely by the freestream. The Stanton number distributions correlate well, consistent with the wall streamlines from the oil film images. The schlieren images document the separation shock, bow shock, and barrel shock. With increasing jet pressure ratios, the separation shock shifts upstream while the bow shock shows a steeper rise and the barrel shock grows substantially in magnitude.

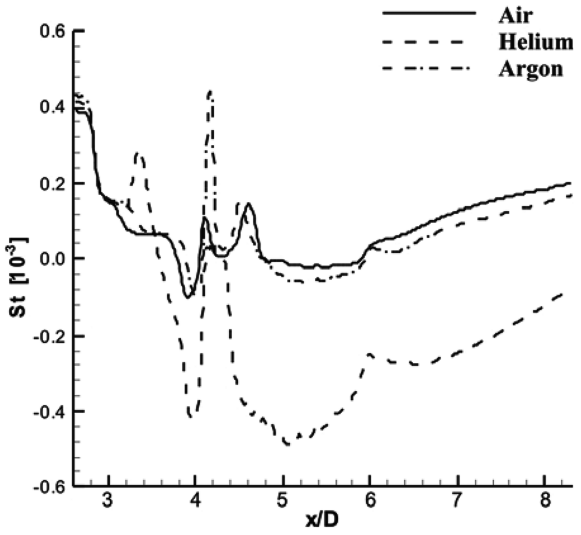

Fig. 19 Stanton numbers measured with different gas jets, $M_\infty = 5.3$, $Re = 12 \times 10^6\ m^{-1}$, $\alpha = 0$ deg, $p_{0J}/p_\infty = 100$, $\varphi = 180$ deg, $T_t = 415$ K.

2) Effect of angle of attack and angle of yaw: With windward injection ($\alpha = -10$ deg), the separation area before the jet is limited to a very small region. The amplitude of the Stanton number peaks in the horseshoe vortex region is five times higher than with the $\alpha = 0$ deg configuration. In a leeward injection ($\alpha = 10$ deg) scenario, the horseshoe vortex extends over a larger area, causing a significant increase in the heat flux. Compared to the $\alpha = 0$ deg setup, an increase by a factor of 15 is observed. In the sideslip configuration ($\beta = 5$, 10 deg, $\alpha = 0$ deg), the asymmetrical flow development around the model surface becomes evident in the Stanton number distribution. In all, the heat flux is greater on the windward side, whereas, on the separated leeward side, the Stanton number profile exhibits substantially smaller values.

3) Effect of helium, argon, and air side jets: The greatly different material properties of the investigated jet gases give rise to substantially altered heat transfer conditions throughout the jet interaction area. Especially in the case of the helium jet, a remarkably reduced heat flux is observed. The Stanton number profile for the argon jet shows its peak amplitude in the horseshoe vortex region, whereas the remainder of the profile corresponds to the air jet results.

References

[1] Cassel, L. A., "Applying Jet Interaction Technology," *Journal of Spacecraft and Rockets*, Vol. 40, No. 4, 2003, pp. 523–537.

[2] Meuer, R., Rosner, N., and Schwenzer, M., "Development of Multiple Supersonic Hot Gas Actuators for Missile Control," Research and Technology Organization MP-23, 1999, pp. 17–29.

[3] Champigny, P., and Lacau, R. G., "Lateral Jet Control for Tactical Missiles," AGARD Rept. 804, 1994, pp. 3-1–3-57.

[4] Seiler, F., Gnemmi, P., Ende, H., Havermann, M., and Schwenzer, M., "Study on Lateral Jet-Crossflow Interaction in the High Energy ISL Shock Tunnel," *23rd International Symposium on Shock Waves*, Deutsch-Französisches Forschungsinstitut PU-628/2001, July 2001.

[5] Fric, T. F., and Roshko, A., "Vortical Structure in the Wake of a Transverse Jet," *Journal of Fluid Mechanics*, Vol. 279, No. 5, 1994, pp. 1–47.
doi:10.1017/S0022112094003800

[6] Steven, J., Henfling, J. F., Erven, R. J., and Spillers, R. W., "Penetration of a Transverse Supersonic Jet into a Subsonic Compressible Cross-Flow," *AIAA Journal*, Vol. 43, No. 2, 2005, pp. 379–389.
doi:10.2514/1.9919

[7] Gruber, M. R., Nejad, A. S., Chen, T. H., and Dutton, J. C., "Large Structure Convection Velocity Measurements in Compressible Transverse Injection Flow-Fields," *Experiments in Fluids*, Vol. 22, Springer–Verlag, Berlin, 1997, pp. 397–407.

[8] Gruber, M. R., Nejad, A. S., Chen, T. H., and Dutton, J. C., "Mixing and Penetration Studies of Sonic Jets in a Mach 2 Free-Stream," *Journal of Propulsion and Power*, Vol. 11, No. 2, 1995, pp. 315–323.
doi:10.2514/3.51427

[9] Qin, N., and Redlich, A., "Massively Separated Flows Due to Transverse Sonic Jet in Laminar Hypersonic Stream," *Shock Waves*, Vol. 9, No. 2, 1999, pp. 87–93.
doi:10.1007/s001930050143

[10] Kovar, A., and Schülein, E., "Comparison of Experimental and Numerical Investigations on Side Jets in a Supersonic Cross-Flow," *Proceedings of the RAeS Aerospace Aerodynamics Research Conference*, Vol. 110, Royal Aeronautical Society, London, 2006, pp. 353–360.

[11] Seiler, F., Gnemmi, P., Ende, H., Schwenzer, M., and Meuer, R., "Jet Interaction at Supersonic Crossflow Conditions," *Shock Waves*, Vol. 13, No. 1, July 2003, pp. 13–23.
doi:10.1007/s00193-003-0189-y

[12] Havermann, M., Ende, H., Seiler, F., and Schwenzer, M., "Shock Tunnel Measurement of the Interaction Amplification Factor for a Hot Gas Side Jet in a Supersonic Cross Flow," *24th International Symposium on Shock Waves*, Deutsch-Französisches Forschungsinstitut PU-642/2004, 2004, pp. 101–107.

[13] Gnemmi, P., and Schäfer, H., "Experimental and Numerical Investigations of a Transverse Jet Interaction on a Missile Body," Deutsch-Französisches Forschungsinstitut, PU-603/2005.

[14] Gnemmi, P., Eichhorn, A., Emunds, H., Esch, H., Gülhan, A., Leopold, F., and Schäfer, H. J., "Experimental and Computational Study of the Interaction Between a Lateral Jet and the Supersonic External Flow on a Generic Missile Body," NATO RTO-AMP-AVT-135, May 2006.

[15] Gruber, M. R., and Goss, L. P., "Surface Pressure Measurement in Supersonic Traverse Injection Flow-Fields," *Journal of Propulsion and Power*, Vol. 15, No. 5, Sept.–Oct. 1999, pp. 633–641.

[16] Henckels, A., and Gruhn, P., "Study on Aerothermal Effects of Viscous Shock Interaction in Hypersonic Inlets," *Proceedings of the 5th European Symposium on Aerothermodynamics for Space Vehicles*, ESA SP-563, 2005, pp. 553–558.

[17] Häberle, J., and Gülhan, A., "Internal Flowfield Investigation of a Hypersonic Inlet at Mach 6 with Bleed," *Journal of Propulsion and Power*, Vol. 23, No. 5, Sept.–Oct. 2007, pp. 1008–1017.

[18] Esch, H., "Die 0.6 m · 0.6 m Trisonische Messstrecke (TMK) des DLR in Köln-Porz (Stand 1986)," DFVLR Mitt. 86-21, 1986.

[19] Stahl, B., Esch, H., and Gülhan, A., "Experimental Investigation of Side Jet Interaction with a Supersonic Cross-flow," *Aerospace Science and Technology*, Vol. 12, No. 4, June 2008, pp. 269–275.
doi:10.1016/j.ast.2007.01.009

[20] Abgrall, R., Desideri, J.-A., Glowinski, R., Mallet, M., and Periaux, J., *Hypersonic Flows for Reentry Problems*, Vol. 3, Springer, Berlin, 1992.

[21] Hitzel, St. M., Hennig, P., and Esch, H., "Navier Stokes Simulation Around a High Velocity Missile with Cross-Flow Jet," *RTO Meeting Proceedings 5*, Missile Aerodynamics, NATO RTO-MP-5, AC/323 (AVT)TP/3, 1998, pp. 17.1–17.112.

[22] Esch, H., "Querschubstrahl-Interferenzen an einem Flugkörperrumpf im Überschall bei unterschiedlichen Ausblasemedien," DLR IB-39113 —99C27, 1999.

[23] Ben-Yakar, A., Mungal, M. G., and Hanson, R. K., "Time Evolution and Mixing Characteristics of Hydrogen and Ethylene Transverse Jets in Supersonic Crossflows," *Physics of Fluids*, Vol. 18, No. 2, 2006, p. 026101.
doi:10.1063/1.2139684

G. Palmer
Associate Editor